Prediction of PCB Field Emissions in Antenna Measurements with an Accelerated Current Reconstruction Method Using Near-Field Data

Robert Nowak, Maximilian Lemke, Stephan Frei

On-board Systems Lab, TU Dortmund University, Germany

robert.nowak@tu-dortmund.de

Abstract — **Estimating the field emission of printed circuit boards (PCBs) early in the development process helps to ensure compliance with limit values in final antenna measurements, to initiate necessary redesign processes and to keep costs low. For this purpose, the use of near-field data is very promising. However, there are many approaches to evaluate near-field data. The current reconstruction method is particularly interesting because it determines physical information of an investigated PCB, e.g., termination impedances of traces, which helps in a precise analysis of critical field sources and their suppression. In this paper, an extension of the current reconstruction method is presented that reduces the computation time without compromising the reconstruction quality. This makes the method applicable to more complex structures. Even for a simple structure, computational time reductions of over 90% are obtained. In addition, the calculated field emission based on the reconstruction results is compared with the results of an antenna measurement. A predominantly good agreement between the predicted and the measured field strength is shown.**

Keywords — **antenna measurement, EMI, near-field, current reconstruction method, source reconstruction, PCB.**

I. INTRODUCTION

Field emission measurements in hardware development processes are typically only performed at the end of the development process due to the time-consuming and cost-intensive antenna measurements required by CISPR 11 [1] or CISPR 25 [2]. To ensure compliance with limit values during final field emission measurements, it is useful to estimate PCB emissions early in the development process. This helps to identify and initiate necessary redesign processes and to keep development costs low. Early predictions of antenna measurement results can be achieved using field simulations or analytical estimates based on measured currents. However, these approaches only yield meaningful results in specific cases. In many cases, the direct measurement of currents on PCBs is limited, and accurate field simulations of PCBs require suitable simulation models, which usually involve a very high modeling effort.

Therefore, near-field techniques are useful for estimating field emission and analyzing internal EMC of PCBs. Here, methods for reconstructing sources are providing promising results. For instance, [3] demonstrates good agreement between the results of antenna measurements and the calculated field of the reconstructed equivalent sources. As stated in [4], this approach can locate the areas of the PCB that contribute to the emission. However, the equivalent sources do not provide any physical information about the actual cause of the field emission. In contrast, current reconstruction methods, as described in [5]-[7], are used to determine the actual current distribution in the traces of the investigated PCB. In addition, the termination impedance of traces can be determined, which allows a targeted redesign of the PCB [8]. Furthermore, the emitted field strengths at any point can also be calculated. Thus, the current reconstruction method can provide more information than equivalent source reconstruction. However, the current reconstruction method requires knowledge of the trace geometry and the material properties of the PCB. This information is necessary to build a model that represents the traces with field sources that apply to transmission line theory. However, the current reconstruction method suffers from long computation times, especially when evaluating phase-less near-field data.

Similar to [9], a reconstructed current distribution is used in this paper to predict the antenna measurement results of a PCB, but it is shown only for a simple single-trace PCB using near-field data with known magnitude and phase. With an extension of the method from [8], the current distribution of a more complex two-trace PCB is reconstructed from phase-less near-field data to predict antenna measurement results. This enhancement significantly reduces the computational time without noticeably degrading the reconstruction quality, and makes the current reconstruction method more practical for use in more complex PCB structures.

This paper consists of four chapters. This introduction is followed by a theory chapter in which the current reconstruction method is briefly presented and the concept of the extension for computational time optimization is introduced. The extension and its application are examined in chapter III. The fourth chapter presents an exemplary study with a validation of the extend current method and a comparison of predicted and measured field emission data. The paper concludes with a summary and an outlook.

II. CURRENT RECONSTRUCTION METHOD AND EXTENSION FOR COMPUTING TIME OPTIMIZATION

The method presented in [7] is the starting point for the extension for computing time optimization introduced in this paper. In this method, the electric and magnetic field data are summarized in the vectors $\mathbf{E}$ and $\mathbf{H}$. These data are used for the current reconstruction of the investigated PCB, which is represented by the vector $\mathbf{I}$. To formulate a relationship between the field data $\mathbf{E}$ and $\mathbf{H}$ and the current distribution $\mathbf{I}$, the PCB traces are divided into sections. Here, the current distribution of each straight-lined section is represented using current waves on the basis of the transmission-line theory. The current on vias is described by constant currents. The matrix $\boldsymbol{\Psi}$ is used to relate the current distribution described in this way to the field data. Here, $\boldsymbol{\Psi}$ is constructed on the basis of field models and the transmission-line theory [7],

$$\boldsymbol{\Psi}_s \cdot \begin{bmatrix} \mathbf{E} \\ \mathbf{H} \end{bmatrix} = \boldsymbol{\Psi}_s \cdot \boldsymbol{\Psi} \cdot \mathbf{I} \tag{1}$$

Besides, the scaling matrix $\boldsymbol{\Psi}_s$ is introduced to scale the electric and magnetic field data:

$$\boldsymbol{\Psi}_s = \begin{bmatrix} \alpha_E \mathbf{I}_{\dim(\mathbf{E})} & \mathbf{0} \\ \mathbf{0} & \alpha_H \mathbf{I}_{\dim(\mathbf{H})} \end{bmatrix}, \ \alpha_E = \frac{1}{\|\mathbf{E}\|}, \ \alpha_H = \frac{1}{\|\mathbf{H}\|}, \tag{2}$$

with the unity matrix $\mathbf{I}_{(\cdot)}$.

In addition to (1), a constraint is formulated on the basis of Kirchhoff's network equations which demands the continuity of currents and voltages at the connection points of all trace sections. For each connection, the equations are summarized in the matrix $\mathbf{K}_C$:

$$\mathbf{K}_C \cdot \mathbf{I} = \mathbf{0}. \tag{3}$$

Refer to [10] for the exact formulation of $\mathbf{K}_C$.

For the current reconstruction, (1) is interpreted as inverse problem using (3) as constraint. As described in [7], this inverse problem is solved several times when evaluating phase-less near-field data. Since for the concrete application of the method more field data $\mathbf{E}$ and $\mathbf{H}$ than unknowns in the vector $\mathbf{I}$ are available, this inverse problem is usually solved using a least squares approach. Thereby, the consideration of the constraint increases the computational effort, as complex solution algorithms are required. This motivates an indirect consideration of the constraint, which is similar to the variable reduction described in [11], which leads to an inverse problem without constraint. This resulting extended inverse problem can be solved with classical least squares algorithms, which optimizes the computation time.

For this purpose, M and N are used to describe the dimension of the matrix $\mathbf{K}_C$ and the vector $\mathbf{I}$:

$$(a) \ \mathbf{K}_C \in \mathbb{C}^{N \times M}, \quad (b) \ \mathbf{I} \in \mathbb{C}^M, \quad N < M. \tag{4}$$

Now, the coefficients of the vector $\mathbf{I}$ are divided into two groups. The first group includes all coefficients by which the current distribution is finally described in the extended inverse problem and thus remain as unknown values. All other coefficients belong to the second group and are characterized by the fact that they can be determined by the variables of the first group and the matrix $\mathbf{K}_C$. Therefore, the coefficients from the second group are referred to as dependent variables and are summarized in the vector $\mathbf{I}_D$. In contrast, the coefficients of the first group are the representative variables and are combined in the vector $\mathbf{I}_R$. The matrices $\mathbf{E}_R$ and $\mathbf{E}_D$ are introduced, to represent the vector $\mathbf{I}$ with $\mathbf{I}_R$ and $\mathbf{I}_D$:

$$\mathbf{I} = \mathbf{E}_R \cdot \mathbf{I}_R + \mathbf{E}_D \cdot \mathbf{I}_D. \tag{5}$$

For this, the columns of the matrices $\mathbf{E}_R$ and $\mathbf{E}_D$ contain only the canonical unit vectors $\mathbf{e}_k$. The concrete structure of the matrices depends on which entries of $\mathbf{I}$ are grouped together in $\mathbf{I}_R$ and $\mathbf{I}_D$. This assignment and the choice of matrices $\mathbf{E}_R$ and $\mathbf{E}_D$ are studied in III. For a better understanding of the procedure, an exemplary choice of matrices is given below:

$$\begin{aligned} (a) \ \ & \mathbf{E}_R = [\mathbf{e}_1 \quad \mathbf{e}_2 \quad \cdots \quad \mathbf{e}_N], \\ (b) \ \ & \mathbf{E}_D = [\mathbf{e}_{N+1} \quad \mathbf{e}_{N+2} \quad \cdots \quad \mathbf{e}_M]. \end{aligned} \tag{6}$$

It applies in principle:

$$(a) \ \mathbf{E}_R \in \mathbb{R}^{M \times (M-N)}, \quad (b) \ \mathbf{E}_D \in \mathbb{R}^{M \times N}. \tag{7}$$

If the identity (5) for $\mathbf{I}$ is placed in the constraint (3), the result is

$$\mathbf{0} = \mathbf{K}_C \cdot \mathbf{E}_R \cdot \mathbf{I}_R + \mathbf{K}_C \cdot \mathbf{E}_D \cdot \mathbf{I}_D. \tag{8}$$

Here, the matrix product $\mathbf{K}_C \cdot \mathbf{E}_R$ has the dimension $N \times N$. If this matrix product is also invertible, then (8) can be transformed to

$$\Leftrightarrow \mathbf{I}_D = -(\mathbf{K}_C \cdot \mathbf{E}_D)^{-1} \cdot \mathbf{K}_C \cdot \mathbf{E}_R \cdot \mathbf{I}_R. \tag{9}$$

This equation is used to calculate the dependent variables $\mathbf{I}_D$ from the representative variables $\mathbf{I}_R$. Additionally, if (9) is used in (5), a calculation rule for $\mathbf{I}$ based on $\mathbf{I}_R$ follows:

$$\mathbf{I} = \underbrace{(\mathbf{E}_R - (\mathbf{K}_C \cdot \mathbf{E}_D)^{-1} \cdot \mathbf{K}_C \cdot \mathbf{E}_R)}_{= \boldsymbol{\Gamma}_R} \cdot \mathbf{I}_R. \tag{10}$$

In this formula, the reduction matrix $\boldsymbol{\Gamma}_R$ is defined. This matrix is used to formulate the extended inverse problem

$$\boldsymbol{\Psi}_s \cdot \begin{bmatrix} \mathbf{E} \\ \mathbf{H} \end{bmatrix} = \boldsymbol{\Psi}_s \cdot \boldsymbol{\Psi} \cdot \boldsymbol{\Gamma}_R \cdot \mathbf{I}_R. \tag{11}$$

In contrast to (1), the classical least squares solution of (11) fulfills the constraint (3).

To evaluate phase-less near-field data with the inverse problem (1) with (3) or (11), the same iterative procedure as in [7] is used. Here, the inverse problem is solved again in each iteration step by using a new, improved reconstruction of the phase information of the near-field data determined in the last iteration step. As in [7] the termination condition of the iteration is formulated based on the mean relative change of two consecutive solutions of $\mathbf{I}$ respective $\mathbf{I}_R$. The iteration ends after 10^5 steps or if the mean relative deviation falls below 10^{-9}. The start value for the iteration is defined as in [7] described where the passivity of the termination is used as a priori information.

III. SELECTION OF THE REPRESENTATIVE CURRENTS FOR THE EXTENSION OF THE INVERSE PROBLEM

Based on a simple investigation of the extended inverse problem, the choice of the matrices $\mathbf{E}_R$ and $\mathbf{E}_D$ is discussed in this chapter. For this purpose, a simple structure is introduced as a case study, which is realized as PCB and investigated with measured data in IV. As shown in Fig. 1, the structure consists of 2 conductors, each with a total length of 100.7 mm and a distance of 1.5 mm. In this chapter, the conductors are round wires with a radius of 0.1 mm in vacuum. The horizontal sections are 1.5 mm above an infinite PEC ground plane, which

is assumed at $z = 0$. To formulate the inverse problem, the conductor is discretized into segments with a maximum length of 0.2 mm. The field data is assumed at the measurement points shown in Fig. 1. The points are located 4 mm above the conductors. Only the z-component of the electric field and the x-component of the magnetic field are being considered. In the formulation (1), vector $\mathbf{I}$ comprises of constant currents $I_{c,(\cdot)}$ for vias, as well as the incident and reflected current waves $I_{i,(\cdot)}$ and $I_{r,(\cdot)}$ for straight-lined sections, as shown in Fig. 1.

The formulation of the extended inverse problem (11) varies depending on the assignments of $I_{c,(\cdot)}$, $I_{i,(\cdot)}$, and $I_{r,(\cdot)}$ to $\mathbf{I}_R$. The resulting formulations are compared based on their condition number. Since the condition number indicates the sensitivity of the solution of an inverse problem to noise in the field data, the condition number of the final formulation should be as small as possible [12]. For the sake of generality, the scaling matrix $\mathbf{\Psi}_s$ is neglected, and only the condition number of $\mathbf{\Psi} \cdot \mathbf{\Gamma}_R$ is evaluated for several exemplary assignments of $I_{c,(\cdot)}$, $I_{i,(\cdot)}$, and $I_{r,(\cdot)}$ to $\mathbf{I}_R$. The resulting condition numbers are shown in Fig. 2 as a function of frequency.

For the most frequencies, the best condition numbers are obtained by assigning only current waves to $\mathbf{I}_R$, as shown by the blue, green, and yellow lines in Fig. 2. It appears that the length

of the section or whether the current waves are from different sections does not affect the results. However, further investigations show an exception to this statement. If the incident (or reflected) current waves of two connected sections are used, e.g. $I_{i,1}$ and $I_{i,2}$, the condition numbers are above 10^{16}. In addition, the constant currents $I_{c,(\cdot)}$, which describe the current on vias, can also be assigned to $\mathbf{I}_R$. Exemplary results for such assignments are given by the magenta, cyan, and purple lines in Fig. 2. Here, the obtained condition number for a combined choice of constant currents and current wave is weaker than using only current waves. However, if only the constant currents at the ends of the conductors are assigned to $\mathbf{I}_R$, a better condition number is obtained for some frequencies than using only current waves. A physical-based explanation for this observation could not be identified. However, subsequent investigation revealed several dependencies associated with this behavior, e.g., the distance between the conductors. Hence, a preferred general choice of the vector $\mathbf{I}_R$ respectively the matrix $\mathbf{E}_D$ cannot be found. Therefore, when formulating the extended problem, it is recommended to evaluate all possible choices of $\mathbf{I}_R$ for each frequency. The matrices $\mathbf{E}_R$ and $\mathbf{E}_D$ that best minimize the condition number of the inverse problem should be used:

$$\min_{\mathbf{E}_R, \mathbf{E}_D}\{\mathrm{cond}(\mathbf{\Psi} \cdot \mathbf{\Gamma}_R)\}. \qquad (12)$$

IV. EXEMPLARY ANALYSIS OF A PCB WITH EXTENDED CURRENT RECONSTRUCTION METHOD

To evaluate the proposed extension, the extend reconstruction method is applied to measurement data and the reconstruction results are analyzed. The next section describes the structure and measurement setup for this investigation. Following that, the performance and results of the reconstruction are analyzed. Finally, field emissions based on the reconstruction results are determined and compared to antenna measurements in section C.

A. Demonstrator PCB and Near-Field Scan

The ideal structure shown in Fig. 1 is realized by microstrips on a PCB with an FR4 substrate and a continuous ground plane at the bottom. This PCB is shown in Fig. 3. In the following, the names of the conductors are L1 and L2. The near-end of the
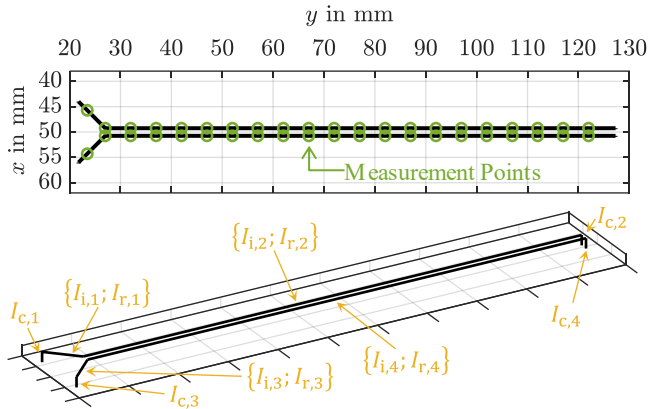

Fig. 1. Structure used for the study with the field data points (top) and the coefficients describing the current distribution (bottom).
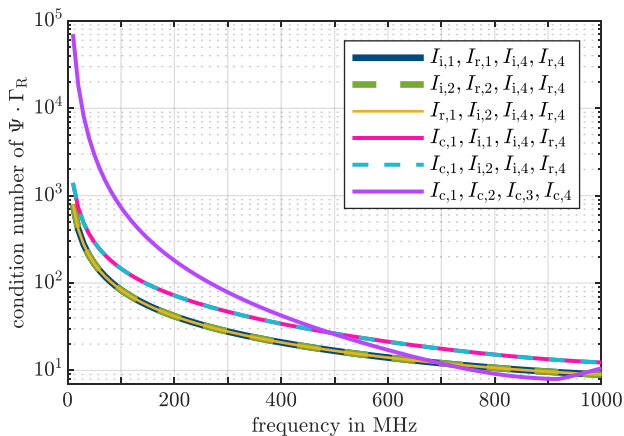

Fig. 2. Comparison of the condition numbers of the inverse problem without the scaling factor from field data for a selection of various choices of $\mathbf{I}_R$.
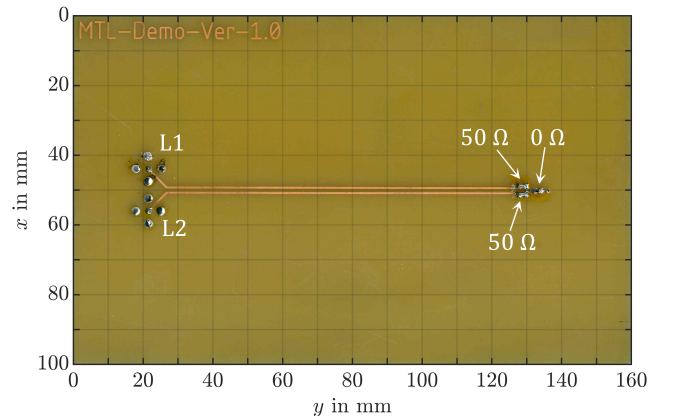

Fig. 3. Used PCB for exemplary analysis.

microstrips is assumed to be at $y \approx 21.75$ mm, and each conductor can be excited via SMB ports on the bottom side. In contrast to the ideal structure shown in Fig. 1, the realization of the far-end at $y \approx 127.3$ mm of the conductors differs. On the PCB, both conductors are terminated by 50 Ω resistors, which are connected to ground with a 0 Ω resistor and a via. The microstrips have a width of 0.6 mm. Thus, a characteristic impedance of approx. 100 Ω and an effective relative permittivity value of 3.1 are assumed for the wave propagation.

A battery-powered sinusoidal signal generator is used to excite the conductors. The frequency of the signals is varied from 30 MHz to 1 GHz with a step size of 10 MHz, and the sinusoidal signal is generated for 3 ms at each frequency. The following excitation scenarios are studied:

- CM (common mode) excitation: Both conductors are connected to one output of the signal generator using a T-shape.
- DM (differential mode) excitation: The conductors are each connected to one output of the signal generator, which generates signals that are shifted by 180°.
- MM (mixed mode) excitation: Same as DM excitation, but a 3 dB attenuator is inserted at the near-end of L2.

As described in III, the near-field is measured at the measurement points shown in Fig. 1. The near-field probes RF-U 2.5-2 and RF-E 10 from Langer EMV-Technik are used to sense the field strengths. The measurement is carried out without phase using the ESRP 3 test receiver from Rohde & Schwarz (TD-Scan, 1 kHz RBW, peak detector, EMI filter). The measurement time is selected with 873 ms in way that three complete sweeps of the excitation can always be measured.

B. Evaluation of the Performance and Calculation Time of the Extended Reconstruction Method

The current distribution is determined using both the original and extended methods for the presented PCB. In this section, the performance of the calculations and the reconstruction results of both methods are compared.

The original and extended methods are each applied 25 times for every frequency, with new initial values generated for each execution. The performance of the computation is measured by monitoring the number of iteration steps n required to satisfy the termination condition. As the number of steps depends on the initial value used, the mean values of the iteration steps for each frequency are compared in Fig. 4. Furthermore, the computation times t of the methods are monitored. Based on these times, the mean computation time reduction Δt_{mean} is determined for each frequency:

$$\Delta t_{\text{mean}} = 1 - \frac{\text{mean}\{t_{\text{extended method}}\}}{\text{mean}\{t_{\text{original method}}\}}. \quad (13)$$

Additionally, the worst-case computation time reduction is determined:

$$\Delta t_{\text{worst-case}} = 1 - \frac{\max\{t_{\text{extended method}}\}}{\min\{t_{\text{original method}}\}}. \quad (14)$$

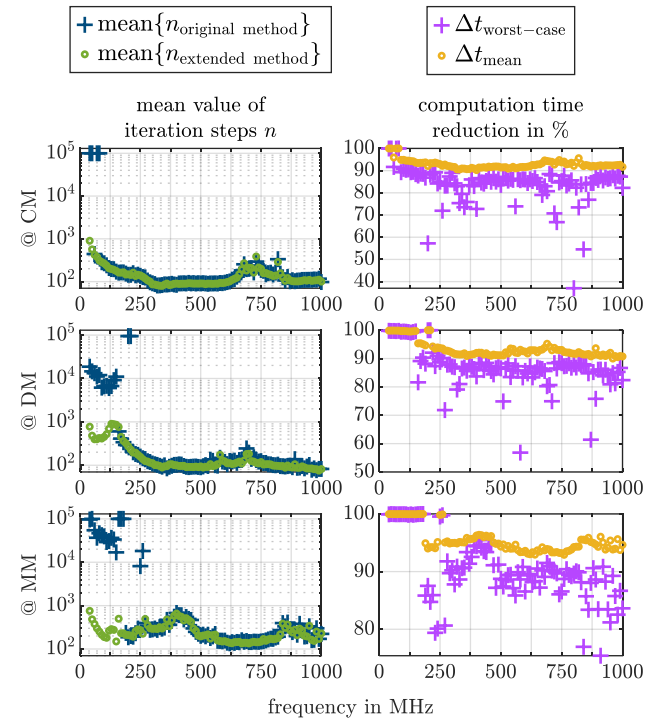These values for the computation time reduction are also shown in Fig. 4.

Fig. 4. Evaluation of the performance of the extended method compared to the original method based on the required number of iteration steps (left) and the reduction in computation time (right).

It is noticeable that the proposed extension improves the convergence of the iterative methods for low frequencies. This is especially significant for the scenarios with DM and MM excitations in the frequency range up to 300 MHz. This improvement can also be observed in the reduction of the computational time. In the mid to high frequency range, the convergence behavior does not seem to be affected by the extension. The improvement in convergence for lower frequencies can also be seen in the speedup. However, it can be seen that the extension reduces the computation time by at least 90% on average. In the worst case, the reduction is mostly above 70%.

In addition, it is examined whether the proposed extension of the method affects the quality of the reconstruction results. For this purpose, the reconstructed input currents at the near ends of conductors L1 and L2 are evaluated. Only the reconstruction results where the termination is passive are considered. For each frequency, the median of these reconstructed currents is determined and shown in Fig. 5. In addition, reference values are determined using scattering parameter measurements. For this purpose, the PCB and the signal generator are characterized with the E5071B network analyzer from Keysight Technologies (IFBW: 100 Hz). The measured output power of the signal generator is used to calculate reference values for the input currents, which are also shown in Fig. 5.

With a few exceptions, there are no significant differences between the reconstruction results of the original methods and the extended method. Therefore, a reduction of the reconstruction quality due to the extension can be excluded. It
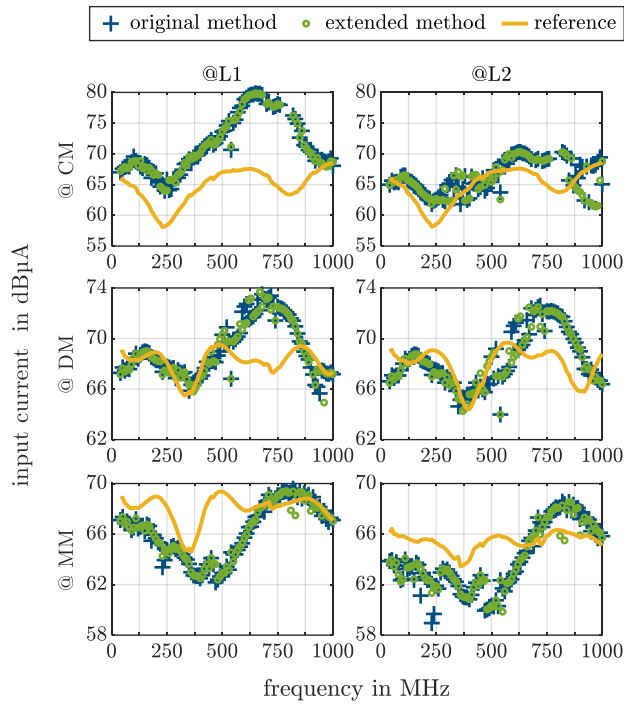
Fig. 5. Reconstructed input current for the conductors L1 and L2 compared to reference values determined by scattering parameters.

can be observed that the deviations of the reconstructed currents from the reference values are less than 6 dB for the scenarios with DM excitation and less than 7 dB for the scenarios with MM excitation. For the CM excitation scenarios, the deviations for the input current L2 are in the same range. Higher deviations are found only for the input current L1, but do not exceed 14 dB.

C. Comparison of the Field Prediction with an Antenna Measurement

The emitted electric field of the PCB can be calculated based on the reconstructed current distribution using the field model of [12]. This section compares this field prediction with antenna measurements.

For this purpose, the electric field strength is determined at the point $(1,52\,\text{m}|0\,\text{m}|0,3\,\text{m})$, referred to the coordinate system of the PCB in Fig. 1, as an example. As a reference, the field strength is measured using an antenna in a semi-anechoic chamber that meets CISPR-25 requirements up to 1 GHz. [2]. This is shown in Fig. 6. The PCB is inserted into an aluminum frame and positioned on a copper table, forming a shield with the ground plane of the PCB in which the signal generator is housed. The table is not connected to the conductive ground of the semi-anechoic chamber to reduce the complexity of the model introduced later. In preliminary tests, the connection between the table surface and the ground has no noticeable effect on the measured field strength. The CBL 6141B antenna from Teseq is used to measure the field strength, with its reference point positioned at the observation point. The distance between the PCB and the antenna tip is 1 m. The ESRP 3 test receiver is used to measure the antenna signal with the parameters mentioned above.
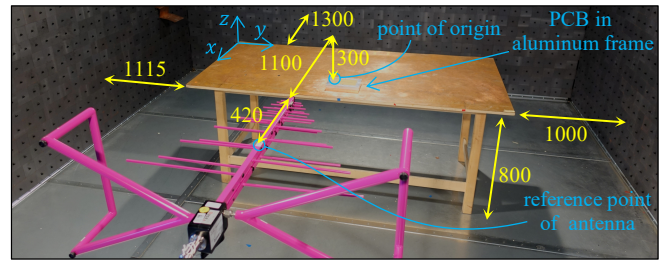

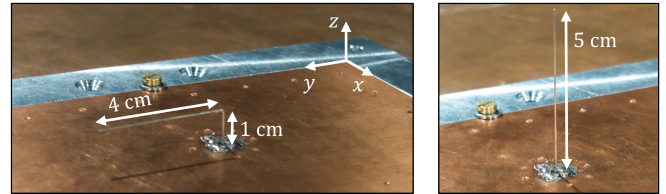Fig. 6. Setup of antenna measurement (distances in mm).

Fig. 7. Horizontal (left) and vertical (right) monopol structures to identify semi-anechoic chamber.
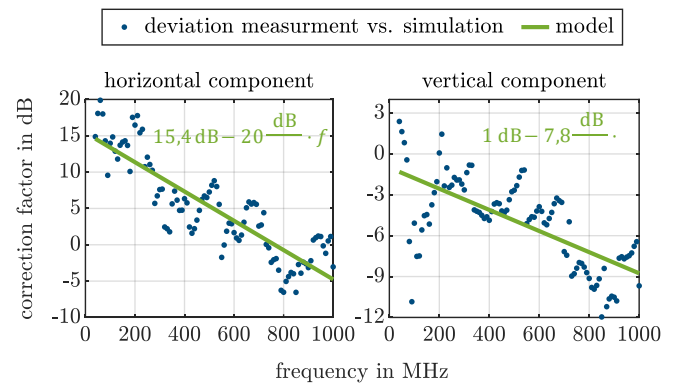

Fig. 8. Correction factor to consider propagation effects in semi-anechoic chamber.

To compare the antenna measurement values with the predicted values based on the current reconstruction, it is necessary to determine the environmental influences of the semi-anechoic chamber. To achieve this, the field of the two monopole structures depicted in Fig. 7 is measured with the antenna and simulated in CONCEPT-II [13]. Each structure is constructed with a round wire that has a diameter of 0.275 mm and is fed with the battery-powered signal generator described above. The simulation assumes that the ground plane of the PCB, on which the monopole structures are built, is an infinite plane, similar to the field model of [12]. Fig. 8 shows the deviations of the horizontal and vertical field strength between the simulation and measurement. Only the horizontal and vertical field components of the respective monopole structures are studied due to their effective emission. Correction factors determined by linear regression based on these deviations are also shown in Fig. 8 and used to correct the measured value.

Fig. 9 shows the predicted and measured emitted electric field strengths. The median values are used for the predicted field, as explained in section IV.B. The predicted and measured values for the horizontal components are predominantly in good agreement for the scenarios with CM and DM excitation.
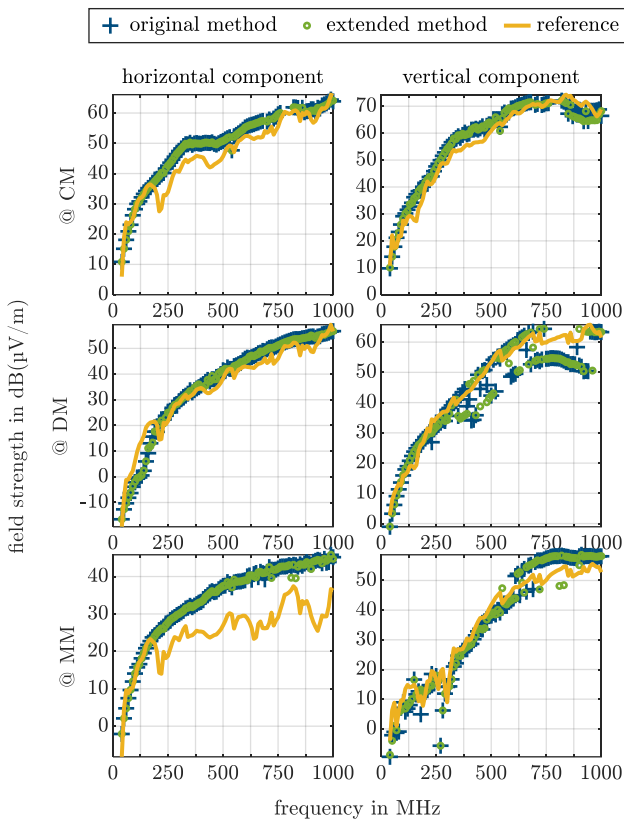
Fig. 9. Measured and predicted field strength.

calculated emission field strength based on these currents are also compared with measured values for different excitation scenarios of the demonstrator PCB. A predominantly good agreement is observed.

Further work could investigate an approach to constrain the correct value when there are ambiguous solutions or predictions. Also, further investigations on the calculated field emission can be done in the next step. Here, the potential of the method to determine compensating effects of different currents should be investigated. This could be combined with the analysis of a more realistic demonstrator.

However, notable deviations are observed in the frequency range from about 200 MHz to 500 MHz for the CM excitation scenario. For the MM excitation scenario, large deviations between predicted field and antenna measurements occur above 200 MHz. In contrast, a good prediction of field strength of the vertical field components can be observed in all scenarios. However, for certain frequencies and scenarios, the predicted values exhibit a second trend line for the emitted field strength. The reason for these ambiguous values is the ambiguous solution space of the iterative algorithm used to evaluate the phase-less near-field data.

It is evident that for both CM and MM scenarios, the field prediction deviates less from the antenna measurement than the reconstructed currents deviate from the reference values in section IV.B. This suggests that while the total currents are accurately determined in these scenarios, the reconstruction of individual conductor currents is only possible in certain scenarios.

V. CONCLUSION AND OUTLOOK

A method for determining the current distribution of a PCB based on phase-less near-field data is presented and extended. The extension reduces the computation time. The application is discussed based on an analytical approach. The reduction of the computation time by at least 90% on average is shown using measured data of a demonstrator PCB with two conductors. An improvement of the convergence of the reconstruction algorithm at low frequencies is observed without a decrease of the reconstruction quality. The reconstructed currents and the

REFERENCES

[1] *Industrial, scientific and medical equipment - Radio-frequency disturbance characteristics - Limits and methods of measurement*, CISPR 11 Ed. 6.2, International Electrotechnical Commission, 2019.

[2] *Vehicles, boats and internal combustion engines - Radio disturbance characteristics – Limits and methods of measurement for the protection of on-board receivers*, CISPR 25 Ed. 5, International Electrotechnical Commission, 2021.

[3] T.-H. Song, X.-C. Wei, J.-J. Ju, W.-T. Liang, and R. X.-K. Gao, "An Effective EMI Source Reconstruction Method Based on Phaseless Near-Field and Dynamic Differential Evolution," *IEEE Trans. Electromagn. Compat.*, vol. 64, no. 5, pp. 1506–1513, Oct. 2022, doi: 10.1109/TEMC.2022.3181142.

[4] Z. A. Wang, J. F. Mao, L. J. Jiang, and P. Li, "Localization and Identification of EMI Sources in Shielding Enclosures Based on a Two-Step Source Reconstruction Method," *IEEE Trans. Electromagn. Compat.*, vol. 65, no. 4, pp. 972–981, Aug. 2023, doi: 10.1109/TEMC.2023.3261400.

[5] H. Weng, D. G. Beetner, R. E. DuBroff, and J. Shi, "Estimation of High-Frequency Currents From Near-Field Scan Measurements," *IEEE Trans. Electromagn. Compat.*, vol. 49, no. 4, pp. 805–815, Nov. 2007, doi: 10.1109/TEMC.2007.908264.

[6] Q. Chen, S. Kato, and K. Sawaya, "Estimation of Current Distribution on Multilayer Printed Circuit Board by Near-Field Measurement," *IEEE Trans. Electromagn. Compat.*, vol. 50, no. 2, pp. 399–405, Jan. 2008, doi: 10.1109/TEMC.2008.921028.

[7] R. Nowak and S. Frei, "Investigation of an Iterative Method for Finding of Currents, Voltages and Termination Impedances of PCB Traces Based on Phase-less Near-field Data," in *2021 IEEE Int. Joint EMC/SI/PI and EMC EUROPE Symp.*, Jul. 2021, pp. 509–514. doi: 10.1109/EMC/SI/PI/EMCEurope52599.2021.9559240.

[8] R. J. Nowak, A. Henke, and S. Frei, "Characterization of EMI Sources from Reconstructed Current Distributions Based on Phase-Less Electric and Magnetic Near-Field Data," in *2020 Int. Symp. on Electromagn. Compat. - EMC EUROPE*, Sep. 2020, doi: 10.1109/EMCEUROPE48519.2020.9245636.

[9] D. Rinas, "Erstellung von Leiterplatten-Abstrahlmodellen unter Beachtung der dominanten Strompfade," Ph.D. thesis, TU Dortmund University, 2018. doi: 10.17877/DE290R-19073.

[10] R. Nowak und S. Frei, "Reconstruction of Current Distribution on a Given Conductor Structure Using Frequency Domain Near-Field Data without Phase Information", in *2019 Int. Symp. on Electromagn. Compat. - EMC EUROPE*, IEEE, Sep. 2019, S. 668–673. doi: 10.1109/EMCEurope.2019.8872074.

[11] P. E. Gill, W. Murray, and M. H. Wright, *Practical optimization*, 11. edition. San Diego: Academic Press, 1997.

[12] D. A. Hill, D. G. Camell, K. H. Cavcey, and G. H. Koepke, "Radiated emissions and immunity of microstrip transmission lines: theory and reverberation chamber measurements," *IEEE Trans. Electromagn. Compat.*, vol. 38, no. 2, pp. 165–172, May 1996, doi: 10.1109/15.494619.

[13] *CONCEPT-II*, Version 12.0 (build no. 53, 2021). Institute of Electromagnetic Theory, Hamburg University of Technology.